Nanoscale

PAPER

View Article Online
View Journal

Cite this: DOI: 10.1039/d5nr05175d

Coupling effects on access resistance of in-series nanopores

Jacob Bair, Thor Burkhardt, Zachery Gottshall and Matthias Kuehne *

We present an analytical model for the electrical resistance of two nanopores in series, where the membrane thickness is considered negligible—a configuration relevant to nanopores in atomically thin 2D materials such as graphene, hexagonal boron nitride, or molybdenum disulfide. We consider an axisymmetric (cylindrical) geometry with a finite-size central compartment separating two non-permselective nanopores and adopt a radial inverse square root current density distribution ($i(r) \propto 1/\sqrt{(1 - r^2/r_n^2)}$) in each nanopore of radius r_n, which we demonstrate is required for accurate quantitative description of the access resistances. Finite element simulations validate the analytical predictions for nanopore-to-central-compartment radius ratios r_n/r_c up to 0.5. Our results accurately describe the crossover from two uncoupled pores in series to a single nanopore as the central compartment length decreases from infinity to zero. We quantify inter-pore coupling *via* a characteristic coupling length ℓ_{95}, defined as the central compartment length at which the total access resistance decreases to 95% of the uncoupled value. We find that ℓ_{95} exhibits a nonlinear dependence on r_n/r_c: for small r_n/r_c ($\lesssim 0.1$), the coupling length can reach up to an order of magnitude greater than r_n, whereas for larger r_n/r_c (approaching 0.5), ℓ_{95} approaches r_n. We additionally find that nanopore coupling is accompanied by a focusing of the current density towards the nanopore center. Our work provides criteria that allow for the better-informed design of nanopores in series devices for use in single biomolecule sensing experiments.

Received 9th December 2025,
Accepted 3rd March 2026

DOI: 10.1039/d5nr05175d

rsc.li/nanoscale

1. Introduction

There is significant interest in the use of nanopores as resistive pulse sensors for single biomolecule detection and characterization.[1–4] While single nanopores have long been used for this purpose, nanopores connected in series are receiving increased attention and various geometries have been investigated, including pore-cavity-pore (through-plane) devices,[5–20] in plane pores in series devices,[21–28] tug-of-war devices,[29–34] and also alternate geometries such as multi-barrel nanopipettes.[35–37] In-series nanopore devices have enabled advanced characterization of various analytes, such as of their electrophoretic mobilites in time-of-flight measurements,[7] the analysis of escape times in narrow escape problems,[6] and the analysis of virus capsid assembly through monitoring of the size of the assembly intermediates.[23,24] In-series nanopores have also enabled the manipulation of the dynamics of particles to allow trapping of molecules in the space between two pores and its use as a reaction chamber to modify the molecules for subsequent characterization,[8,20] and it has been proposed that a pores-in-series geometry would allow the separation of polymers by length.[13]

Resistive pulse sensing and the design of the devices that are meant to carry it out requires knowledge of the conductance, or equivalently the resistance, of the nanopore system. For a single nanopore, the total resistance is usually treated as the bulk resistance of the system plus an additional term, the access resistance, which arises from the convergence of the charge carrier streamlines to each side of the pore. The contribution to the access resistance from one side of a single circular nanopore with radius r_n has previously been established as[38]

$$R_a = \frac{\rho_{bulk}}{4r_n} \quad (1)$$

in the limit where the pore is contacted on each side by a semi-infinite electrolyte reservoir. However, if finite sized external reservoirs are considered, the access resistance associated with these external reservoirs may differ significantly from eqn (1). This has been shown explicitly for long, rectangular nanopores ("nanochannels") connected to microchannel compartments.[39] Such finite size effects on the access resistance are expected to be more important in cylindrical geometries.[39] In addition to the outer compartments, for a two nanopores in series device, the finite size of the

Department of Physics, Brown University, Providence, RI 02912, USA.
E-mail: kuehne@brown.edu

central compartment may also have pronounced effects on the access resistance.

Herein we present an analytical model for the electrical resistance of two nanopores in series as schematically shown in Fig. 1 for the case of no surface charge on the pores so that they are not permselective. We consider the case of negligible thickness of the membranes in which the nanopores are embedded. This most closely resembles the important case of nanpores in 2D materials such as graphene, hexagonal boron nitride, or various transition metal dichalcogenides such as molybdenum disulfide (MoS_2), which are attractive not only for their high mechanical strengths and chemical durabilities, but also for their unique transport properties arising from their minimal thickness and the effects of surface charge.[40–48] While surface charge effects can be significant in such nanopores, particularly at low ionic strengths, we focus here on the limit where these effects are negligible, allowing us to isolate the geometric contributions to the access resistance. The use of nanopores in 2D materials has also recently been demonstrated in nanopore in series devices for trapping and enhanced temporally and spatially resolved tracking of DNA.[19,20] We compare the predictions of this analytical model to the results of finite element simulations and identify a coupling regime for which the resistance of the system is no longer well approximated with the use of eqn (1) for the access resistance on both sides of each pore. We then comment on the limitations of the validity of the analytical model as revealed by the simulations and discuss the aspects of the analytical model that may be useful in the design of nanopores in series devices for the detection of single molecules.

2. Analytical model

We consider two nanopores connected in series as represented by the axisymmetric 3-compartment model depicted in Fig. 1 in the limit of vanishing permselectivity. To keep the system analytically tractable, we assume two nanopores of equal radius r_n and negligible length l_n centered on the z-axis. The two nanopores are separated by a central compartment of length l_c and radius r_c. We consider each nanopore to be further connected to an exterior compartment as would be the case in a nanofluidic experiment. We consider similarly sized exterior compartments of length l_m and radius $r_m = l_m$. A voltage difference ΔV is applied across the model, with the top side held at $-\frac{\Delta V}{2}$ and the bottom side at $\frac{\Delta V}{2}$. The compartments are filled with a symmetric, monovalent, binary electrolyte characterized by its bulk resistivity

$$\rho_{bulk} = \frac{k_B T}{c_0 2e^2 D}, \tag{2}$$

where k_B is Boltzmann's constant, T is the temperature of the system, c_0 is the salt concentration, e is the elementary charge, and D is the diffusion coefficient (assumed identical for the two ions). The outer walls of all of the channels are assumed to be rigid and impermeable.

We use a continuum-based approach and assume a sufficiently dilute electrolyte solution such that the steady-state convectionless transport of ions in our system is governed by the Poisson–Nernst–Planck (PNP) equations (see eqn (39) and (40)). In the limit of vanishing permselectivity considered

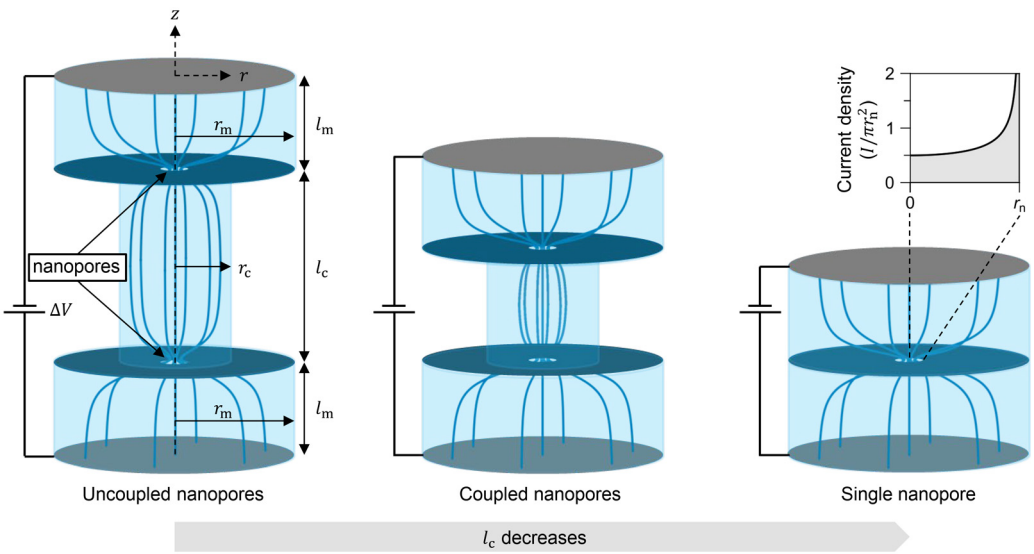

Fig. 1 Schematic of the nanopores-in-series configuration considered in this work (not to scale) when the length l_c of the central compartment is long enough that the two pores are essentially uncoupled (left), when l_c is small so that the associated access resistances are noticeably reduced (center), and the limiting case where $l_c = 0$, and the system becomes a single nanopore (right). The two pores are assumed to have equal radii r_n and connect to exterior electrolyte compartments of macroscopic length l_m and radius $r_m = l_m \gg r_n$. Streamlines of the ionic current resulting from a potential difference ΔV applied across each model are included. The inset shows the assumed radial inverse square root dependence of the current density in each nanopore, eqn (11).

here—corresponding to zero surface charge on the pore walls—the local ion concentration remains uniform throughout the system and equal to the bulk concentration, c_0. Under these conditions, the PNP equations reduce to Laplace's equation for the electric potential

$$\nabla^2\phi = 0 \tag{3}$$

in each region. We therefore seek the solution to Laplace's equation for the specified geometry that satisfies all of the appropriate boundary conditions. It is important to note that, due to the use of the PNP framework, the model can only be expected to hold down to pore sizes of approximately 1–2 nm. For smaller pores, continuum assumptions may break down and the Poisson–Nernst–Planck equations will no longer remain valid, although the exact limit for the validity of the PNP equations is still an active area of research.[49–51] Ion-ion correlations may also violate the PNP framework at electrolyte concentrations upwards of 0.1 M.[49]

2.1. Case of a single nanopore

We first consider the limiting case of a single nanopore where $l_c = 0$ as shown in Fig. 2. We define the bottom edge of the system to be located at $z = 0$ in a cylindrical coordinate system and first consider the solution in the region $0 \le z \le l_m$. The solution to Laplace's equation for this geometry is given by[52]

$$\phi(r,z) = A + Bz + \sum_{g=1}^{\infty} a_g J_0(k_g r)\sinh(k_g z) \tag{4}$$

where J_0 is the zeroth-order Bessel function and A, B, a_g, and k_g are undetermined coefficients to be obtained from the relevant boundary conditions. In the macroscopic exterior compartment, we have

$$\phi(r,0) = \frac{\Delta V}{2} \tag{5}$$

and require no flux of the electric potential through the compartment walls so that

$$\left.\frac{\partial\phi}{\partial r}\right|_{r=r_m} = 0 \tag{6}$$

From eqn (5) and (6) we obtain $k_g = \beta_g/r_m$ and $A_m = \Delta V/2$, where β_g is the gth positive zero of the first order Bessel function, $J_1(x)$. At $z = l_m$, the electrical current density through the nanopores is given by

$$i(r) = -\frac{1}{\rho_{bulk}}\left(\frac{\partial\phi}{\partial z}\right) \tag{7}$$

The impermeable walls enforce $i(r) = 0$ outside the nanopore, so that

$$\left.\frac{\partial\phi}{\partial z}\right|_{z=l_m} = \begin{cases} -\rho_{bulk} i(r) & 0 \le r < r_n \\ 0 & r_n \le r \le r_m \end{cases} \tag{8}$$

Integrating each side of this expression over the proper domains gives

$$B = -\rho_{bulk}\frac{I}{\pi {r_m}^2} \tag{9}$$

where I is the total current flowing through the system.

Using the orthogonality of Bessel functions, we can multiply eqn (8) by $J_0(\beta_{g'} r/r_m)$ and integrate each side of the equation over the proper domains to solve for each $a_{g'}$ individually. To solve for these coefficients, however, we first need to know the form of the current density in the nanopore, $i(r)$. At this point, a constant current density given by

$$i(r) = \frac{I}{\pi {r_n}^2} \tag{10}$$

could be assumed, which has worked well before with individual, in parallel, and asymmetric four-layered nanochannel systems where l_n is very large compared to r_n under the assumption that, analogous to fluid flow through pipes, the large length of the channel allows the current streamlines to fully develop to become parallel and evenly spaced.[39,53,54] However, for our system, since we consider the case where l_n is negligible, it is unreasonable to assume that the current streamlines will become fully developed so that there is a constant current density in the nanopores. In fact, it has been shown that the assumption of a uniform current density is not sufficient to predict transition times in the chronopotentiometric response of permselective membranes and is therefore not a good assumption in modeling ionic transport in electrochemical systems, and that the correct current density must increase near the boundary of the pores.[55] An additional discussion can be found in section S1 of the SI where we show that, even for very long nanochannels, the assumption of a

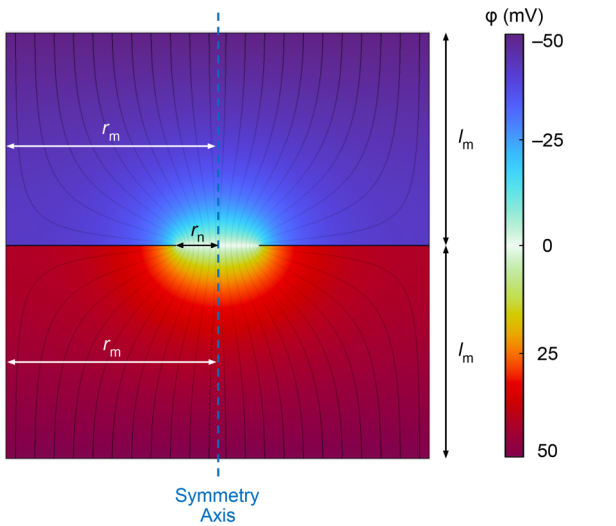

Fig. 2 The case of a single pore of radius r_n. The pore connects two compartments of radius r_m and length l_m. The top side of the system is held at $-\Delta V/2$ and the bottom side is held at $\Delta V/2$. Equipotential false coloring and current streamlines are shown.

uniform current density should not be expected to hold. To find a more appropriate form for the current density within the pore, we note that the access resistance problem of a single nanopore of negligible thickness between two infinitely sized electrolyte reservoirs maps to the problem of electrical current flow through a circular constriction between two infinitely sized electrical conductors. Instead of a constant current density, we turn to a radial inverse square root dependence that has been established for this problem in electrical contact theory by directly solving Laplace's equation for the case where $r_n/r_m \to 0$, which is given by the expression[56]

$$i(r) = \frac{I}{2\pi {r_n}^2 \sqrt{1 - r^2/{r_n}^2}} \tag{11}$$

Eqn (11) has been shown to be a good approximation for the current density in a constriction as long as the radius of the constriction is less than about half of the radius of the adjoining compartments, $r_n \lesssim 0.5 r_m$.[57] It is worth noting here that at $r = r_n$ the approximated current density given by eqn (11) diverges. The singularity is simply a consequence of the sharp edge geometry of the system and is expected due to the sudden change in boundary conditions at r_n. For a real system, the singularity would be regularized as real edges cannot be infinitely sharp due to atomic scale roughness. Using the radial inverse square root current density and carrying out the integration as described yields

$$a_{g'} = -\frac{\rho_{bulk} I \sin(\beta_{g'} r_n/r_m)}{\pi r_n \beta_{g'}{}^2 J_0{}^2(\beta_{g'}) \cosh(\beta_{g'} l_m/r_m)} \tag{12}$$

Having solved for all of the coefficients, we now shift the origin of the z-axis to be located at the plane of the nanopore so that, due to the symmetric geometry of the system, the antisymmetry of the electric potential requires $\phi(r,0) = 0$. Using this condition at $r = 0$, we arrive at the expression for the resistance of the entire system,

$$R = \Delta V/I = R_{bulk} + 2R_a \tag{13}$$

where the bulk resistance term is given by

$$R_{bulk} = \frac{2\rho_{bulk} l_m}{\pi {r_m}^2} \tag{14}$$

and the access resistance R_a, which arises on both sides of the nanopore, is given by

$$R_a = \sum_{g=1}^{\infty} \frac{\rho_{bulk} \sin(\beta_g r_n/r_m) \tanh(\beta_g l_m/r_m)}{\pi r_n \beta_g{}^2 J_0{}^2(\beta_g)} \tag{15}$$

For comparison, we can also solve for the resistance of the system with the assumption of a uniform current density. To do so, we simply replace $i(r)$ in eqn (8) with the form given by eqn (10). From there, the calculation is the same as for the case with the inverse square root current density. The expression for B is still given by eqn (9). To solve for the coefficients $a_{g,const}$, we multiply the modified eqn (8) by $J_0(\beta_{g'} r/r_m)$ and once again integrate over the proper domains to obtain

$$a_{g',const} = -\frac{2\rho_{bulk} I J_1(\beta_{g'} r_n/r_m)}{\pi r_n \beta_{g'}{}^2 J_0{}^2(\beta_{g'}) \cosh(\beta_{g'} l_m/r_m)} \tag{16}$$

for the coefficients. The total resistance for the system under the assumption of a constant current density is therefore

$$R_{const} = \Delta V/I = R_{bulk} + 2R_{a,const} \tag{17}$$

where the bulk resistance term is again given by eqn (14) and the access resistance, $R_{a,const}$, which arises on both sides of the nanopore, is given by

$$R_{a,const} = \sum_{g=1}^{\infty} \frac{2\rho_{bulk} J_1(\beta_g r_n/r_m) \tanh(\beta_g l_m/r_m)}{\pi r_n \beta_g{}^2 J_0{}^2(\beta_g)} \tag{18}$$

The form of this solution is almost the same as the form of eqn (15) but with the $\sin(\beta_g r_n/r_m)$ term replaced with $2J_1(\beta_g r_n/r_m)$. Therefore, while the dependence of the access resistance on the ratio of the size of the nanopore to the size of the adjoining compartments is different for each of the two models, the assumption of a radial inverse square root current density predicts the same dependence of the access resistance on the ratio of the longitudinal and transverse dimensions of the adjoining compartments that is predicted using the assumption of a uniform current density within the pore. This dependence of the access resistance on the ratio of the dimensions of the adjoining compartments is in agreement with several previous studies for nanochannel geometries that assume uniform current densities at the mouths of the channels.[52,58–65]

Since we are generally concerned with the case where $l_m \geq r_m \gg r_n$, we have $\beta_g \frac{l_m}{r_m} > \beta_g > \beta_1$ so that $\tanh\left(\beta_g \frac{l_m}{r_m}\right) \geq \tanh(\beta_1) = 0.999$. It is therefore safe to set $\tanh(\beta_g l_m/r_m) \approx 1$ for all g in eqn (15). As $r_m \to \infty$, for the argument in the sine term, $r_n/r_m \approx 0$ so that $\sin\left(\beta_g \frac{r_n}{r_m}\right) \approx 0$ except for when β_g becomes very large. We further note that in the limit of high g, $\beta_g \approx \pi(g + 1/4) \approx \pi g$ and that, for $x \to \infty$, $J_0(x) \to \sqrt{\frac{2}{\pi x}} \cos\left(x - \frac{\pi}{4}\right)$.[66] We therefore have $\beta_g{}^2 J_0{}^2(\beta_g) \approx 2(g + 1/4) \approx 2g$. It can then be shown through evaluation of a well-known Fourier series that

$$\lim_{l_m, r_m \to \infty} R_a = \lim_{r_m \to \infty} \left[\frac{\rho_{bulk}}{\pi r_n} \sum_{g=1}^{\infty} \frac{\sin\left(\pi g \frac{r_n}{r_m}\right)}{2g} \right] = \frac{\rho_{bulk}}{4 r_n}, \tag{19}$$

recovering eqn (1), *i.e.*, the established access resistance of a circular nanopore in contact with a semi-infinite electrolyte reservoir,[38] as expected. Similarly, we can consider the limiting behavior for the access resistance derived using the assumption of a constant current density, as given by eqn (18). Using the same approximations that were used for the case of the radial inverse square root current density along with the inte-

gral representation of the first order Bessel function, $J_1(x) = \frac{1}{\pi}\int_0^\pi \sin\theta \sin(x\sin\theta)\mathrm{d}\theta$, we can once again reduce the limit to an evaluation of a well-known Fourier series to arrive at

$$\lim_{l_m, r_m \to \infty} R_{a,const} = \lim_{r_m \to \infty}\left[\frac{\rho_{bulk}}{\pi r_n}\sum_{g=1}^{\infty}\frac{J_1\left(g\pi\frac{r_n}{r_m}\right)}{g}\right] = \frac{\rho_{bulk}}{\pi r_n}, \quad (20)$$

which is larger than the expected expression, eqn (1). The failure of eqn (18) to exhibit the correct limiting behavior for $r_m, l_m \to \infty$ demonstrates that a uniform current density is indeed a bad assumption when considering pores of negligible thickness.

2.2. Case of two nanopores in series

We now move on to the case where $l_c \neq 0$ so that we now have two nanopores connected in series. The system is symmetric about a plane perpendicular to the axis of symmetry and running through the middle of the central compartment, which we define to exist at $z = 0$. We consider only the solution in the half-space $z \leq 0$. The solution to Laplace's equation in each region for this geometry is again given by eqn (4). We approach this problem by separately solving for the potential in each of the two compartments existing in the half-space, the lower exterior compartment and the lower half of the central compartment, separately and subsequently matching the solutions at $z = -l_c/2$ to obtain the relationship between the applied voltage and the current. Using the same assumption of a radial inverse square root current density in the pores, for the outer macroscopic compartment, the boundary conditions remain the same as for the case of a single pore but with the z-coordinates shifted by $l_m + l_c/2$. Therefore, we have $k_{g,m} = \beta_g/r_m$, $B_m = \rho_{bulk} I/{r_m}^2$, $A_m = \Delta V/2 - \rho_{bulk} I(2l_m + l_c)/2\pi{r_m}^2$, and

$$a_{g',m} = -\frac{\rho_{bulk} I \sin(\beta_{g'} r_n/r_m)}{\pi r_n \beta_{g'}{}^2 J_0{}^2(\beta_{g'})\cosh(\beta_{g'} l_m/r_m)} \quad (21)$$

where the subscript 'm' indicates that we are considering the solution in the macroscopic exterior compartment, $-(2l_m + l_c)/2 \leq z \leq -l_c/2$. We now consider the solution for the potential in the bottom half of the central compartment. Due to the symmetric geometry of the system, the electric potential will be antisymmetric, $\phi(r,-z) = -\phi(r,z)$, so that, for the portion of the central compartment that exists in the half-space $z \leq 0$, we have

$$\phi_c(r, 0) = 0 \quad (22)$$

where the subscript 'c' indicates that we are considering the solution in the bottom half of the central compartment, $-l_c/2 \leq z \leq 0$. Again, we require no flux of the electric potential through the compartment walls so that

$$\left.\frac{\partial \phi_c}{\partial r}\right|_{r=r_c} = 0 \quad (23)$$

from which we obtain $k_{g,c} = \beta_g/r_c$ and $A_c = 0$.

At $z = -l_c/2$, the electrical current density through the nanopores is given by

$$i(r) = -\frac{1}{\rho_{bulk}}\left(\frac{\partial \phi_c}{\partial z}\right) \quad (24)$$

so that, in combination with the condition of impermeable walls,

$$\left.\frac{\partial \phi_c}{\partial z}\right|_{z=-l_c/2} = \begin{cases} -\rho_{bulk} i(r) & 0 \leq r < r_n \\ 0 & r_n \leq r \leq r_c \end{cases} \quad (25)$$

Integrating over the proper domains gives

$$B_c = -\rho_{bulk}\frac{I}{\pi {r_c}^2} \quad (26)$$

and, by assuming the radial inverse square root current density given by eqn (11), we can multiply eqn (25) by $J_0(\beta_{g'} r/r_c)$ and once again integrate to solve for each $a_{g',c}$ individually to yield

$$a_{g',c} = -\frac{\rho_{bulk} I \sin(\beta_{g'} r_n/r_c)}{\pi r_n \beta_{g'}{}^2 J_0{}^2(\beta_{g'})\cosh(\beta_{g'} l_c/2r_c)} \quad (27)$$

We now have the solution for the electric potential in both compartments. Matching the solutions at the boundary where the nanopore connects the two compartments

$$\phi_m\left(r, -\frac{l_c}{2}\right) = \phi_c\left(r, -\frac{l_c}{2}\right) \quad (28)$$

we arrive at the expression for the resistance of the entire system

$$R = \Delta V/I = R_{bulk} + 2R_{a,c} + 2R_{a,m} \quad (29)$$

where the bulk resistance term is given by

$$R_{bulk} = \frac{\rho_{bulk} l_c}{\pi {r_c}^2} + 2\frac{\rho_{bulk} l_m}{\pi {r_m}^2} \quad (30)$$

and the access resistances $R_{a,c}$ and $R_{a,m}$, which arise on both sides of each nanopore, are given by

$$R_{a,c} = \sum_{g=1}^{\infty}\frac{\rho_{bulk}\sin(\beta_g r_n/r_c)\tanh(\beta_g l_c/2r_c)}{\pi r_n \beta_g{}^2 J_0{}^2(\beta_g)} \quad (31)$$

and

$$R_{a,m} = \sum_{g=1}^{\infty}\frac{\rho_{bulk}\sin(\beta_g r_n/r_m)\tanh(\beta_g l_m/r_m)}{\pi r_n \beta_g{}^2 J_0{}^2(\beta_g)} \quad (32)$$

As was done for the case of a single pore, for comparison, we may solve for the resistance of the two pore system under the assumption of a constant current density. The calculation proceeds in exactly the same was as for the case with the inverse square root current density but with $i(r)$ replaced by

eqn (10) instead of eqn (11). The coefficients remain exactly the same with the exception of

$$a_{g',\mathrm{c,const}} = -\frac{2\rho_{\mathrm{bulk}} I J_1(\beta_{g'} r_\mathrm{n}/r_\mathrm{c})}{\pi r_\mathrm{n} \beta_{g'}{}^2 J_0{}^2(\beta_{g'}) \cosh(\beta_{g'} l_\mathrm{c}/2r_\mathrm{c})} \tag{33}$$

and

$$a_{g',\mathrm{m,const}} = -\frac{2\rho_{\mathrm{bulk}} I J_1(\beta_{g'} r_\mathrm{n}/r_\mathrm{m})}{\pi r_\mathrm{n} \beta_{g'}{}^2 J_0{}^2(\beta_{g'}) \cosh(\beta_{g'} l_\mathrm{m}/r_\mathrm{m})} \tag{34}$$

Matching the solutions at the boundary gives

$$R_\mathrm{const} = \Delta V/I = R_\mathrm{bulk} + 2R_\mathrm{a,c,const} + 2R_\mathrm{a,m,const} \tag{35}$$

where the bulk resistance term is again given by eqn (30) and the access resistances, $R_\mathrm{a,c}$ and $R_\mathrm{a,m}$, which arise on both sides of each nanopore, are given by

$$R_\mathrm{a,c,const} = \sum_{g=1}^{\infty} \frac{2\rho_{\mathrm{bulk}} J_1(\beta_g r_\mathrm{n}/r_\mathrm{c}) \tanh(\beta_g l_\mathrm{c}/2r_\mathrm{c})}{\pi r_\mathrm{n} \beta_g{}^2 J_0{}^2(\beta_g)} \tag{36}$$

and

$$R_\mathrm{a,m,const} = \sum_{g=1}^{\infty} \frac{2\rho_{\mathrm{bulk}} J_1(\beta_g r_\mathrm{n}/r_\mathrm{m}) \tanh(\beta_g l_\mathrm{m}/r_\mathrm{m})}{\pi r_\mathrm{n} \beta_g{}^2 J_0{}^2(\beta_g)} \tag{37}$$

Again, these forms are almost the same as the form of eqn (31) and (32) but with the $\sin(\beta_k r_\mathrm{n}/r_\mathrm{m})$ terms replaced with $2J_1(\beta_g r_\mathrm{n}/r_\mathrm{m})$.

Eqn (32) is exactly the same expression as eqn (15) so that the limit of $R_\mathrm{a,m}$ as $l_\mathrm{m}, r_\mathrm{m} \to \infty$ is again $\rho_{\mathrm{bulk}}/4r_\mathrm{n}$. Note that for $r_\mathrm{m}, l_\mathrm{m} \to \infty$, if we let $l_\mathrm{c} \to 0$ in eqn (31), we obtain $R = R_\mathrm{bulk} + 2R_\mathrm{a,m} = R_\mathrm{bulk} + \frac{\rho_{\mathrm{bulk}}}{2r_\mathrm{n}}$. In other words, if the central compartment vanishes, the system we recover is that of a single nanopore with its two associated access resistances (see Fig. 1 right). Note also that eqn (31) and (32) are identical in the case where $r_\mathrm{c} = r_\mathrm{m}$ and $l_\mathrm{c} = 2l_\mathrm{m}$. In this case, and for $r_\mathrm{m}, l_\mathrm{m} \to \infty$, we obtain $R = R_\mathrm{bulk} + 4R_\mathrm{a,m} = R_\mathrm{bulk} + \frac{\rho_{\mathrm{bulk}}}{r_\mathrm{n}}$, *i.e.*, the access resistance contributions to the total resistance are those of two uncoupled nanopores each in contact with semi-infinite electrolyte reservoirs on both sides.

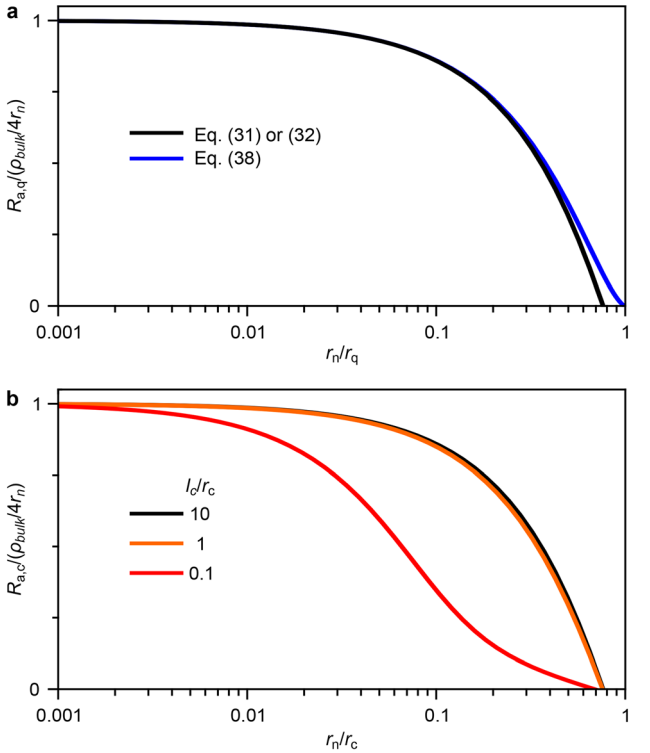

Fig. 3 (a) Access resistance as given by eqn (31), $q = c$, or eqn (32), $q = m$, in the uncoupled pore limit ($l_\mathrm{c} \to \infty$) plotted with respect to $r_\mathrm{n}/r_\mathrm{c}$ and normalized by $\rho_{\mathrm{bulk}}/4r_\mathrm{n}$ (black). Rosenfeld and Timsit's[67,68] result based on a more accurate radial current density (eqn (38), blue). (b) Access resistance as given by eqn (31) plotted as a function of $r_\mathrm{n}/r_\mathrm{c}$ and normalized by $\rho_{\mathrm{bulk}}/4r_\mathrm{n}$ for different values of the relative central compartment length $l_\mathrm{c}/r_\mathrm{c}$.

drops. The dependence we derive based on the inverse square root form of the current density in the nanopore (eqn (11)) is shown in black in Fig. 3a. It compares very well with the more accurate dependence (blue line in Fig. 3a) derived by Rosenfeld and Timsit[67,68] for the case of a constriction in an infinite cylindrical conductor without the assumption of a specific current density in the constriction
in the relevant range $r_\mathrm{n}/r_\mathrm{m} \leq 0.5$ (respectively $r_\mathrm{n}/r_\mathrm{c} \leq 0.5$) where

$$R_\mathrm{a,Timsit} = \frac{\rho_{\mathrm{bulk}}}{4r_\mathrm{n}} \left[1 - 1.41581\left(\frac{r_\mathrm{n}}{r_\mathrm{m}}\right) + 0.06322\left(\frac{r_\mathrm{n}}{r_\mathrm{m}}\right)^2 + 0.15261\left(\frac{r_\mathrm{n}}{r_\mathrm{m}}\right)^3 + 0.19998\left(\frac{r_\mathrm{n}}{r_\mathrm{m}}\right)^4\right] \tag{38}$$

We further explore the dependence of the access resistances given by eqn (31) and (32) on the ratios $r_\mathrm{n}/r_\mathrm{c}$ and $r_\mathrm{n}/r_\mathrm{m}$, respectively. In Fig. 3a, we consider the uncoupled nanopore limit ($l_\mathrm{c}, l_\mathrm{m} \to \infty$) so that the hyperbolic tangent terms in the expressions for the access resistance are set equal to 1. For $r_\mathrm{n} \ll r_\mathrm{m}$ (respectively $r_\mathrm{n} \ll r_\mathrm{c}$), we recover $R_\mathrm{a,m} \approx \rho_{\mathrm{bulk}}/4r_\mathrm{n}$ (respectively $R_\mathrm{a,c} \approx \rho_{\mathrm{bulk}}/4r_\mathrm{n}$), *i.e.*, the expected expression of the access resistance associated with a nanopore in contact with a semi-infinite electrolyte reservoir (eqn (1)). However, as the nanopore radius becomes comparable to the radius of the neighboring compartment, the associated access resistance the inverse square root current density is supposed to hold well. For ratios greater than 0.5, the access resistance given by eqn (38) approaches 0 while the access resistance given by eqn (31) and (32) tend towards negative values.

Next, we explore the access resistance in the central compartment as we vary l_c. Eqn (31) predicts the dependencies shown in Fig. 3b. As can be seen, while for $l_\mathrm{c}/r_\mathrm{c} \gg 1$ we obtain the same trend as shown in Fig. 3a, for $l_\mathrm{c}/r_\mathrm{c} < 1$ we see a pronounced reduction in $R_\mathrm{a,c}$ down to small ratios of $r_\mathrm{n}/r_\mathrm{c}$. This is the hallmark effect of interpore coupling on the access resistance in the central compartment.

3. Numerical computation

In order to validate our analytical results, we performed numerical simulations across a range of geometries using the finite element solver COMSOL. A voltage difference of ΔV = 0.1 V was chosen for the simulations so that the top side of the system was held at 0.05 V and the bottom side of the system was held at −0.05 V. Since the simulations required a finite length of the nanopores, the length was chosen so that $l_n/2r_n \ll 1$ in order to mimic the results for a true constriction of zero length. The outer walls of the channels were set to be rigid and impermeable so that $\vec{J}_\pm \cdot \vec{n} = 0$, where $\vec{J}_\pm$ represents the fluxes of the positive and negative ion species and $\vec{n}$ is the unit vector normal to the channel walls. The bulk concentration was set to be C = 10 mol m^{-3}. For all simulations, the charge numbers of the two ion species were chosen to be $z_\pm$ = ±1. The transport of ions in the simulations was then governed by Poisson's equation

$$\nabla^2\phi = -\frac{\rho}{\varepsilon} \tag{39}$$

and the steady state Nernst–Planck equation

$$\vec{J}_\pm = -D_\pm\left(\vec{\nabla}c_\pm \pm \frac{e}{k_B T}c_\pm\vec{\nabla}\phi\right) \tag{40}$$

Values of $D_\pm$ = 1.0 × 10^{-9} m^2 s^{-1} for the ion diffusivities, close to that of the constituent ions in many dilute aqueous monvalent salt solutions, T = 293.15 K for the temperature, and ε_r = 80 for the relative permittivity of the fluid, the approximate value for an aqueous electrolyte, were chosen for the simulations. To reduce the computational complexity of our simulations, we chose values of $r_m = l_m$ on the order of several nanometers, noting that as long as $r_m = l_m \gg r_n$ the contribution to the total access resistance from these exterior compartments should remain well approximated by eqn (1) and will therefore be similar to that of exterior compartments of larger dimensions. These equations constitute the Poisson–Nernst–Planck (PNP) framework for ion transport, which forms the basis for validating our analytical model. Note that for the zero surface charge conditions considered here, the simulations confirm that the concentration remains uniform throughout the domain, consistent with the assumptions underlying the analytical derivation.

4. Results

Before examining the results of the simulations, we first present the expected behavior of the access resistance as described by our analytical model. For the design of nanopores in series devices it is important to have a thorough understanding of the impact that the design parameters will have on the resistance of the device. We therefore wish to determine the degree of nanopore coupling *via* the lengths ℓ_p at which the total access resistance, $\sum R_a = 2R_{a,c} + 2R_{a,m}$, has dropped to a percent value p = 97.5, 95, 90, 85, 80, 75 of its uncoupled value (the value obtained for $l_c \to \infty$ in Fig. 3). The top of Fig. 4 shows the dependency of the ratio ℓ_p/r_c on the ratio r_n/r_c for different values of p as predicted from eqn (31) and (32), where we have set $l_m = r_m = r_c$. As p decreases, the values of ℓ_p/r_c decrease as well, with the relationship between ℓ_p/r_c and p being nonlinear. Less of a decrease in ℓ_p/r_c is required to achieve the same decrease in p as the value of p decreases. This behavior indicates that, even for l_c just below that which results in a reduction of the access resistance by 5%, the access resistance becomes very sensitive to small changes in l_c.

Further insight can be gained by considering the relationship between ℓ_p and r_n as r_n/r_c changes. The slopes of the curves in the top of Fig. 4 approach unity for small values of r_n/r_c, meaning that, for these small values of r_n/r_c, the ratio of ℓ_p to r_n will be a constant that is dependent on the chosen value of p. The saturation of the curves in the bottom of Fig. 4

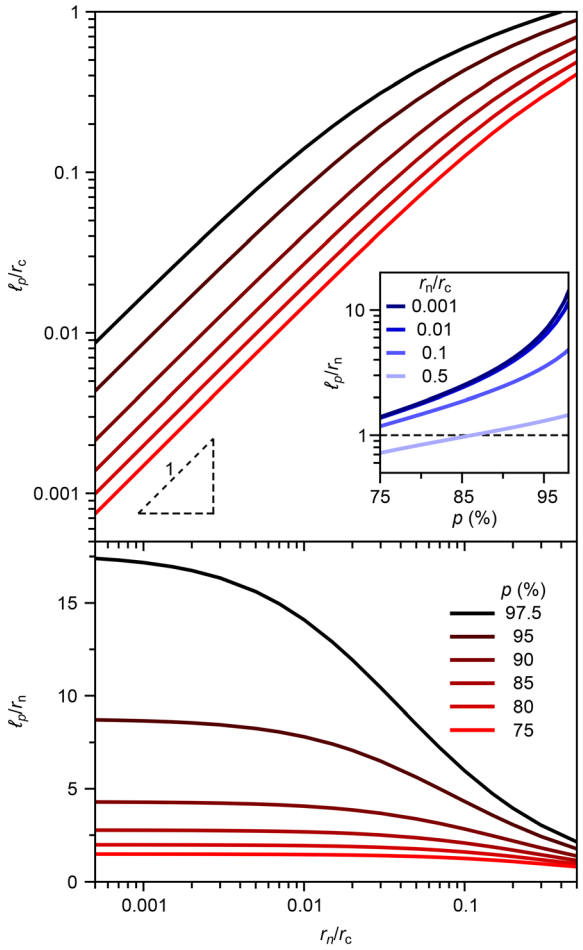

Fig. 4 Characteristic nanopore coupling length, ℓ_p, normalized by r_c (top) and r_n (bottom) and plotted as a function of r_n/r_c, where p is the percentage of the uncoupled value of $R_{a,c}$ (obtained in the limit where $l_c \to \infty$). The inset shows ℓ_p normalized by r_n as a function of p for different r_n/r_c.

at low values of r_n/r_c highlights this effect, as well as the non-linear behavior in the inset at the top of Fig. 4 for small r_n/r_c. Additionally, the bottom of Fig. 4 shows that, regardless of the value of p, for r_n/r_c approaching 0.5, ℓ_p will be very close to the dimensions of the nanopore. This effect is highlighted by the inset in the top of Fig. 4. Similarly, Chou *et al.*[19] recently defined the coupling length for two asymmetric nanopores in series as the length at which the total conductance of the system departs from the uncoupled reference case, *i.e.*, where the two nanopores are spaced apart by a length significantly greater than their dimensions. In this case, Chou *et al.*[19] found numerically that coupling occurs when the separation between nanopores is roughly the same as their diameters. Our model and definition of nanopore coupling predict similar coupling lengths for $r_n/r_c \gtrsim 0.1$. However, as can be seen in Fig. 4, for small values of r_n/r_c nanopore coupling noticeably reduces the access resistance in the central compartment already at lengths ℓ_p up to an order of magnitude greater than r_n. To achieve ~25% reduction in access resistance compared to the uncoupled pore case, we nonetheless need $l_c \approx r_n$.

Having established the expected behavior of the resistance of the system, we now present the results of the finite element method simulations. These results are divided into two distinct cases. We first present results for the case where the radius of the central channel matches the radius of the two exterior compartments in section 4.1. In section 4.2, we present the results when the radius of the central channel is allowed to vary.

4.1. Case I: $r_c = r_m$

Fig. 5a shows an example of one of the geometries considered for this case with $r_c = r_m = 40$ nm, $r_n = 8$ nm, and $l_c = 80$ nm. The equipotential false coloring and current streamlines were extracted from the simulation data. For this case, r_c was always set equal to r_m and r_n/r_c, was allowed to vary up to 0.5. The length of the central compartment, l_c, was varied as well.

The total access resistance, $\sum R_a = 2R_{a,c} + 2R_{a,m}$, was obtained from the simulation data by subtracting the bulk resistance from the total resistance of the system. In Fig. 5b, the total access resistance as a function of the central channel length ranging from 2 nm to 200 nm is plotted for r_n/r_c ratios of 0.025, 0.05, 0.1, 0.3, and 0.5. The total access resistances computed from eqn (31) and (32) are shown by the solid lines in the figure, and the total access resistances computed from the same model but using the uniform current density described by eqn (10) are shown by the dashed lines in the figure. The access resistance approaches the expected value equal to that of two completely independent nanopores each in contact with semi-infinite electrolyte reservoirs on both sides at large values of l_c, and drops towards the value expected for a single pore in contact with semi-infinite electrolyte reservoirs on both sides as l_c decreases. The values obtained from eqn (31) and (32) agree well with the simulated data with a slight deviation at low values of l_c and provide a much better match to the data than the values obtained using the assumption of a uniform current density.

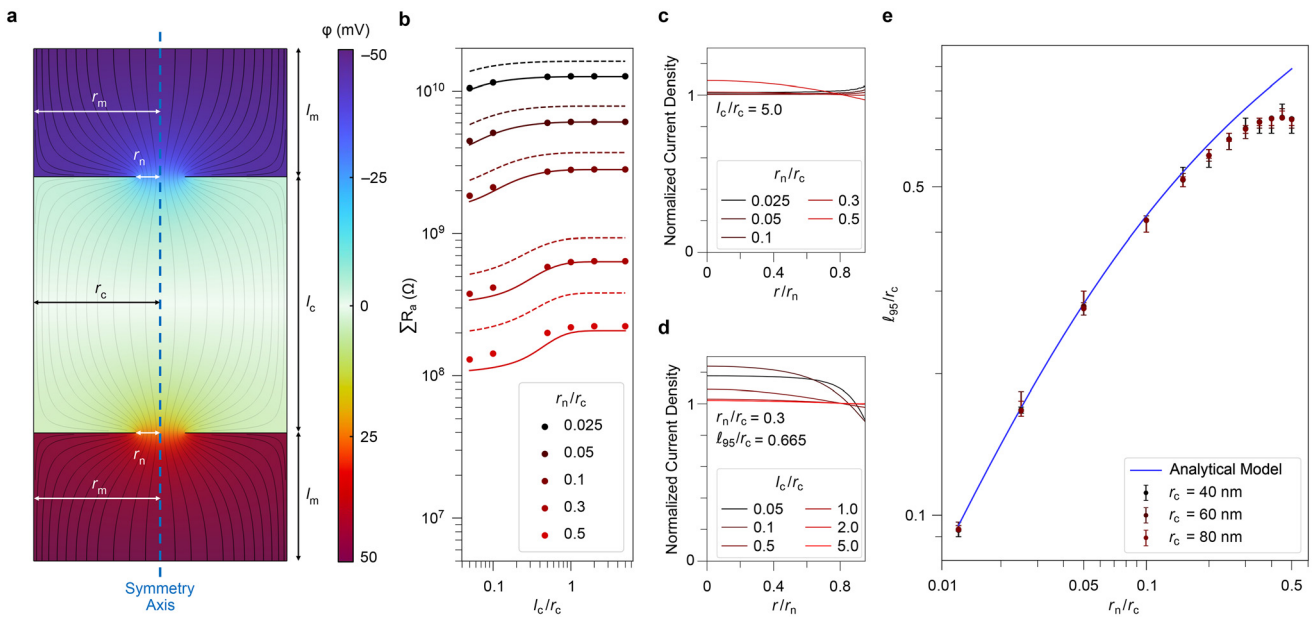

Fig. 5 Simulation results for Case I where $r_c = r_m$. (a) System cross section with equipotential false coloring and current streamlines for $r_n/r_c = 0.2$ and $l_c/r_c = 2.0$. (b) Total access resistance for various ratios of r_n/r_c compared to the predictions of the model assuming either an inverse square root current density (eqn (11), solid lines) or a constant current density (eqn (10), dotted lines). (c) The current density in the nanopore normalized by eqn (11) for various values of r_n/r_c when $l_c/r_c = 5.0$. (d) The normalized current density for various values of l_c/r_c and constant $r_n/r_c = 0.3$. (e) Normalized coupling length for different values of $r_c = r_m$ as a function of r_n/r_c plotted alongside the predictions of the analytical model.

The current densities, $i(r)$, in the nanochannels are also extracted from the simulation data. Fig. 5c shows the current density normalized by eqn (11) as a function of the normalized radius, r/r_n, for a set value of l_c = 200 nm and for r_n/r_c ratios of 0.025, 0.05, 0.1, 0.3, and 0.5. Note that in Fig. 5c, the graph is cut off near $r/r_n = 1$, since, for $r/r_n \to 1$, the current density given by eqn (11) approaches infinity. In the region that has been cut from the graph, the normalized current density rapidly approaches zero. The data shows that the current density in the pore is in good agreement with the assumed form of the current density for ratios of r_n/r_c less than 0.5, at which point more of the current density spreads towards the center of the nanopore as opposed to being concentrated towards the edge and the deviation of the current density from the approximated form begins to become significant. Fig. 5d shows the current density normalized by eqn (11) as a function of the normalized radius, r/r_n, for a set value of r_n = 12 nm and for l_c values of 2 nm, 4 nm, 20 nm, 40 nm, 80 nm, and 200 nm, where again the graph has been cut off near $r/r_n = 1$ due to the divergence of eqn (11) for $r/r_n \to 1$. For large values of l_c, the current density agrees very well with the form given by eqn (11). As l_c decreases, the current density begins to deviate from the approximate form by focusing more towards the center of the pore, reaching a maximum point of deviation and then tending back towards the form of eqn (11) as the geometry begins to approach that of a single pore. The deviation from the assumed current density corresponds to the deviation of the simulation extracted total access resistances from those expected from the model for small values of l_c.

We arbitrarily define the coupling length to be ℓ_{95}, the length at which the total access resistance drops to 95% of the saturated value for large l_c, as beyond this 5% deviation, the total access resistance drops rapidly and the effects of the coupling cannot be ignored. Additionally, a 5% reduction is significant as it represents a reasonable threshold that may be experimentally distinguished from spurious effects related to tolerances and noise. We extract the coupling length as a function of the nanopore radius for $r_c = r_m$ = 40 nm, 60 nm, and 80 nm and plot it in Fig. 5e. The data collapses onto the same curve for the three different values of $r_c = r_m$ showing that, for this geometry, the coupling condition is influenced only by the ratio of the nanopore radius to the radius of the central channel, since for this geometry the radius of the central channel and the radius of the exterior compartment are set to be the same. For the specific geometry considered in Fig. 5d, the ratio of the coupling length to the radius of the central compartment is 0.665. For l_c/r_c above this value, the current density in the nanopores matches very well with the approximated form, while for ratios below this value, focusing of the current density towards the center of the nanopore occurs, showing that the coupling of the nanopores not only reduces the access resistance but is also accompanied by a deviation of the current density from the form given by eqn (11).

4.2. Case II: varying r_c

Fig. 6a shows an example of a geometry considered for this second case with r_m = 40 nm, r_c = 20 nm, r_n = 2 nm, and l_c = 40 nm. The equipotential false coloring and current streamlines were extracted from the simulation data. For this case, r_c was varied between 10 nm and 40 nm, and r_n/r_c was allowed to

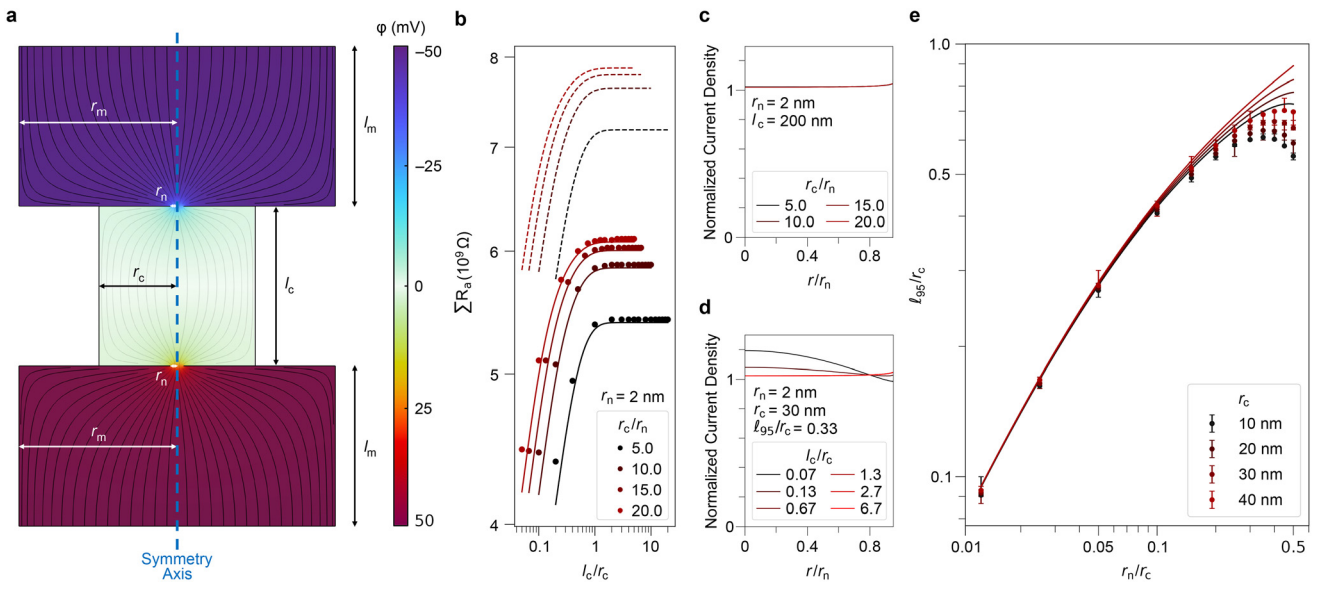

Fig. 6 Simulation results for Case II where $r_c \neq r_m$ = 40 nm. (a) System cross section with equipotential false coloring and current streamlines for r_c/r_n = 10.0 and r_n = 2 nm. (b) Total access resistance for various ratios of r_c/r_n and constant r_n compared to analytical predictions assuming either an inverse square root current density (eqn (11), solid line) or a constant current density (eqn (10), dotted line). (c) The current density in the nanopore normalized by eqn (11) for several values of r_c/r_n and constant r_n and l_c. (d) The normalized current density for several values of l_c/r_c and constant r_n and r_c. (e) Normalized coupling lengths for different values of r_c plotted alongside the predictions of analytical model.

vary up to 0.5. The length of the central channel, l_c, was also varied. The value of r_m was kept constant at 40 nm.

Again, the total access resistance was obtained from the simulation data by subtracting the bulk resistance from the total resistance. In Fig. 6b, the total access resistance as a function of the central channel length ranging from 2 nm to 200 nm is plotted for a constant value of r_n = 2 nm and values of r_c = 10 nm, 20 nm, 30 nm, and 40 nm. The total access resistances computed from eqn (31) and (32) are shown by the solid lines in the figure, and the total access resistances computed from the same model using the uniform current density are shown by the dashed lines. For all values of r_c, the access resistance drops towards the expected value for a single pore in contact with semi-infinite electrolyte reservoirs on both sides as l_c decreases. However, as r_c decreases, the total access resistance no longer approaches that of two completely independent nanopores each in contact with semi-infinite electrolyte reservoirs on both sides, even for large values of l_c, as the effect of a finite sized central channel remains important for these smaller values of r_c. Again, the values obtained from eqn (31) and (32) agree with the simulated data with a slight deviation at low values of l_c and provides a better description than the model using the assumption of a uniform current density in the pore.

The current densities in the nanochannels were again extracted from the simulation data for this second case. Fig. 6c shows the current density normalized by eqn (11) as a function of the normalized radius for set values of l_c = 200 nm and r_n = 2 nm and for r_c/r_n ratios of 5.0, 10.0, 15.0, and 20.0. As was done for previous graphs of current densities normalized by eqn (11), the graph in Fig. 6c is cut off near $r/r_n = 1$ due to the divergence of eqn (11) when $r/r_n \to 1$. In all cases, the current density in the pore is in good agreement with the assumed form of the current density, as the ratio of r_n to r_c remains well below the value of 0.5 at which the validity of the approximation begins to break down. Fig. 6d shows the normalized current density as a function of the normalized radius for set values of r_n = 2 nm and r_c = 30 nm and for l_c values of 2 nm, 4 nm, 20 nm, 40 nm, 80 nm, and 200 nm where we have once again excluded the region of the graph near $r/r_n = 1$. For large values of l_c, the current density agrees very well with the form given by eqn (11). As l_c decreases, the current density begins to focus more towards the center of the pore, corresponding to the deviation of the access resistances obtained from the simulations from those obtained from the model for small values of l_c as seen in Fig. 6b.

We extract the coupling length as a function of the nanopore radius and plot it for values of r_c = 10 nm, 20 nm, 30 nm, and 40 nm in Fig. 6e. For this plot, we normalize both the coupling length and the nanopore radius by the radius of the central channel, and the value of the radius of the exterior compartments is kept constant at r_m = 40 nm. The curves for the different central channel radii take a similar shape, but are compressed as the radius decreases. As expected, the coupling length therefore becomes dependent on both r_c/r_m and r_n/r_m in addition to the ratio r_n/r_c. For the specific geometry considered in Fig. 6d, the ratio of the coupling length to the radius of the central compartment is 0.33. As was seen for the first case, for l_c/r_c above this value the current density in the nanopores matches very well with the approximated form, while for ratios below this value, noticeable focusing of the current density towards the center of the nanopore occurs.

5. Discussion

Our results provide an accurate description of the access resistance of a nanopores in series pair from which the correct ratios can be determined to either achieve or avoid coupling of the pores in the design of nanopores in series devices. The analytical model is limited by the validity of approximating the current density in the nanopores by eqn (11), which we have shown works well for ratios of r_n/r_c up to 0.5, in agreement with previous findings.[57,67,68] The results show that, as expected, the simplified assumption of a constant current density cannot be used. We also demonstrate that the coupling regime is characterized by a focusing of the current density from the edges of the pores to their centers, leading to slight deviations from the predictions of our model. Accurate determination of the access resistance in nanopores in series systems is therefore strongly dependent on the determination of the correct current density within the pores, and an interesting direction for future work could be the determination of a more accurate description of the current density for both the case where $r_c \neq r_m$ and the cases where r_n/r_c and r_n/r_m may be greater than 0.5.

We note that the current density focusing reported here arises naturally from the geometry of the system. A physical explanation for the focusing of the current density in the coupling regime can be found by considering the spreading of the current in the central channel. As the length of the central channel decreases, the electrical resistance penalty incurred as a consequence of spreading radially throughout the compartment becomes very large in comparison to the resistance associated with remaining close to the system's center. Therefore, the density of the current streamlines at the center of the system increases as the two pores approach, as more of the current will flow along the paths of lower resistance. Fig. 7 shows the current density in the middle of the central compartment (z = 0) for a typical geometry that was studied, which drops rapidly to zero for values of r greater than r_n at small values of l_c, illustrating this tendency for more of the current to remain closer to the system's center. The reduction in the spreading of the current causes the access resistance to decrease and leads to the coupling behavior present in both the simulations and the analytical model. It follows that the greater deviation of the current density in the nanopores from the approximated form at small values of l_c also arises from this focusing of the current density in the central channel towards the radial center of the system. The radial inverse square root current density was derived for the case of a constriction between two infinitely sized electrical conductors[56]

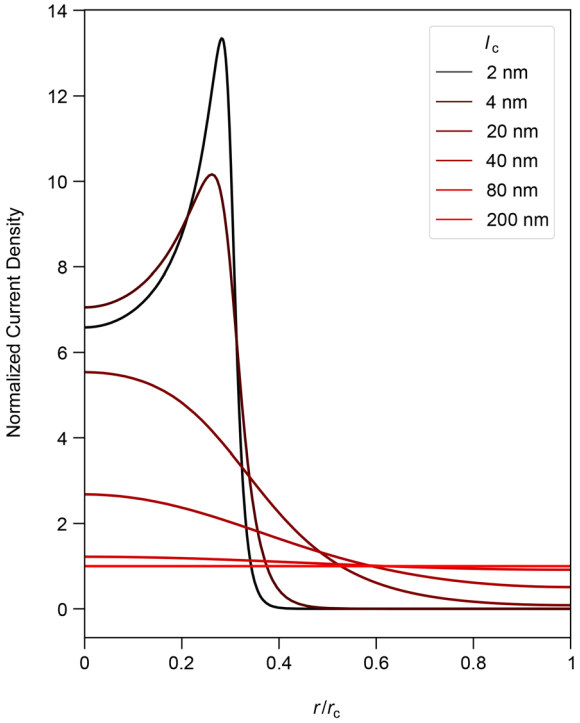

Fig. 7 Current density in the middle of the central channel, normalized by $I/\pi r_c^2$, for different lengths of the central compartment. Here r_n = 12 nm and $r_m = r_c$ = 40 nm.

and therefore is expected to break down when these conductors, or equivalently the electrolyte compartments surrounding the pores in our system, become finite in size and the spreading of the current becomes limited. When the current density is kept radially more collimated in the space between the pores, the current density near the radial center of the pores gets enhanced compared to the radial inverse square root approximation. Essentially, since the current remains concentrated mostly near the center of the system, the central channel has an effective radius that is no longer much larger than the radius of the nanopore, leading to a focusing effect that is similar to what can be seen in Fig. 5c for $r_n/r_c = 0.5$.

In addition to being characterized by a deviation of the current density in the nanopores from the form of eqn (11), the coupling is also characterized by a high sensitivity to changes in l_c/r_c. The high sensitivity of the resistance to changes in the geometry of the system within this coupling regime could be taken advantage of in the design of nanofluidic sensing devices. Additionally, the value for ℓ_{95}/r_c peaks at a specific value of r_n/r_c. The value of r_n/r_c where this maximum coupling length occurs is an important parameter in the design of coupled nanopores in series devices, as it sets an upper limit on what the separation length may be for the pores to remain coupled as well as what the size of the pores must be to achieve this length. While the analytical model predicts a peak in the value of ℓ_{95}/r_c as well, the model predicts these peaks to occur for higher values of r_n/r_c and overestimates the coupling length near $r_n/r_c = 0.5$ due to the deviation in the actual current density from the radial inverse square root form that was assumed.

While we assume the pores to have a negligible thickness in our model to approximate the case of nanopores in 2D materials, in real systems and for very small pores, the radius of the pore may approach the finite thickness of many 2D materials. As discussed in section S2 of the SI, the model we derive under the assumption of negligible thickness still works well provided that the bulk resistance from the nanopores is included in the expression for the total resistance of the system.

Our model is also derived under the assumption of vanishing permselectivity (zero surface charge), which ensures uniform ion concentration throughout the system. As described in more detail in section S3 of the SI, the model can still be expected to hold for low values of the surface charge density at concentrations such that the Dukhin length is very small compared to the radius of the pore. For nanopores with significant surface charge, particularly at low salt concentrations where the Debye length becomes comparable to the pore dimensions, permselectivity effects would need to be incorporated. The extension of this framework to account for surface charge and permselective effects represents an important direction for future work.

6. Conclusions

In this work we have derived analytical expressions for the electrical resistance of two nanopores in series for the case of vanishing permselectivity and negligible pore thickness. The model adopts a radial inverse square root current density profile within the pores, which we demonstrate is essential for accurate quantitative predictions—in contrast to the constant current density assumption often used for long nanochannels. We validate our analytical model against finite element simulations and show good agreement for nanopore-to-central-compartment radius ratios r_n/r_c up to 0.5. Our model correctly recovers the expected limiting behaviors: as the central compartment length $l_c \to 0$, the system reduces to a single nanopore with its two associated access resistances; as $l_c \to \infty$, the resistance approaches that of two uncoupled nanopores; and for $r_n \ll r_c$ (respectively $r_n \ll r_m$), the access resistance reduces to Hall's classical result, $\rho_{bulk}/4r_n$. We quantify inter-pore coupling through a characteristic coupling length, ℓ_{95}, at which the total access resistance decreases to 95% of the uncoupled value. This coupling length exhibits a nonlinear dependence on r_n/r_c: for small r_n/r_c ($\lesssim 0.1$), ℓ_{95} can reach up to an order of magnitude greater than r_n, whereas for larger r_n/r_c (approaching 0.5), ℓ_{95} approaches r_n. We additionally find that nanopore coupling is accompanied by a focusing of the current density from the pore edges toward the center, and that the access resistance becomes highly sensitive to small changes in l_c within the coupling regime. Our results provide a framework for determining the resistance of nanopores in series systems and can be used to extract design parameters for the construction

of coupled and uncoupled nanopore devices for single biomolecule manipulation, sensing, and characterization.

Author contributions

Jacob Bair: data curation (lead), investigation (equal), formal analysis (lead), writing – original draft (lead), writing – review & editing (equal). Thor Burkhardt: investigation (equal), formal analysis (supporting), writing – review & editing (equal). Zachery Gottshall: investigation (equal), formal analysis (supporting), writing – review & editing (equal). Matthias Kuehne: conceptualization (lead), investigation (equal), formal analysis (supporting), funding acquisition (lead), project administration (lead), supervision (lead), writing – original draft (supporting), writing – review & editing (equal).

Conflicts of interest

The authors have no conflicts to disclose.

Data availability

The data that support the findings of this study are available in Zenodo, at https://doi.org/10.5281/zenodo.18940627.[69]

Supplementary information (SI) is available. See DOI: https://doi.org/10.1039/d5nr05175d.

Acknowledgements

This work is based on a project supported by a Seed Research Award from the Brown University Initiative for Sustainable Energy (ISE). T.B. acknowledges support through an Undergraduate Teaching and Research Awards (UTRA) fellowship from the Brown University Summer/Semester Projects for Research, Internship, and Teaching (SPRINT) program.

References

1 C. Dekker, *Nat. Nanotechnol.*, 2007, **2**, 209–215.
2 D. Kozak, W. Anderson, R. Vogel and M. Trau, *Nano Today*, 2011, **6**, 531–545.
3 L. Xue, H. Yamazaki, R. Ren, M. Wanunu, A. P. Ivanov and J. B. Edel, *Nat. Rev. Mater.*, 2020, **5**, 931–951.
4 Y.-L. Ying, Z.-L. Hu, S. Zhang, Y. Qing, A. Fragasso, G. Maglia, A. Meller, H. Bayley, C. Dekker and Y.-T. Long, *Nat. Nanotechnol.*, 2022, **17**, 1136–1146.
5 D. Pedone, M. Langecker, A. M. Münzer, R. Wei, R. D. Nagel and U. Rant, *J. Phys.: Condens. Matter*, 2010, **22**, 454115.
6 D. Pedone, M. Langecker, G. Abstreiter and U. Rant, *Nano Lett.*, 2011, **11**, 1561–1567.
7 M. Langecker, D. Pedone, F. C. Simmel and U. Rant, *Nano Lett.*, 2011, **11**, 5002–5007.
8 X. Liu, M. M. Skanata and D. Stein, *Nat. Commun.*, 2015, **6**, 6222.
9 G. Sampath, *RSC Adv.*, 2015, **5**, 30694–30700.
10 G. Sampath, *RSC Adv.*, 2015, **5**, 167–171.
11 W. Dunbar and J. Kim, Dual-pore device, *U.S. Patent* 8961763, 2015, https://lens.org/054-804-249-903-364.
12 M. Magill, C. Falconer, E. Waller and H. W. de Haan, *Phys. Rev. Lett.*, 2016, **117**, 247802.
13 M. Magill, E. Waller and H. W. de Haan, *J. Chem. Phys.*, 2018, **149**, 174903.
14 W. Dunbar and J. Kim, Dual-pore device, *U.S. Patent* 9863912, 2018, https://lens.org/106-479-442-511-838.
15 K. Briggs, G. Madejski, M. Magill, K. Kastritis, H. W. de Haan, J. L. McGrath and V. Tabard-Cossa, *Nano Lett.*, 2018, **18**, 660–668.
16 C. Liao, F. Antaw, A. Wuethrich and M. Trau, *Adv. Mater. Technol.*, 2020, **5**, 2000701.
17 X. S. Ling, *Quant. Biol.*, 2020, **8**, 187–194.
18 R. Zando, M. Chinappi, C. Giordani, F. Cecconi and Z. Zhang, *Nanoscale*, 2023, **15**, 11107–11114.
19 Y.-C. Chou, C.-Y. Lin, A. Castan, J. Chen, R. Keneipp, P. Yasini, D. Monos and M. Drndić, *Nat. Nanotechnol.*, 2024, **19**, 1686–1692.
20 W. Xu, C. Ma, G. Wang, F. Fu and J. Sha, *Nanotechnology*, 2024, **35**, 335302.
21 Z. D. Harms, K. B. Mogensen, P. S. Nunes, K. Zhou, B. W. Hildenbrand, I. Mitra, Z. Tan, A. Zlotnick, J. P. Kutter and S. C. Jacobson, *Anal. Chem.*, 2011, **83**, 9573–9578.
22 Z. D. Harms, D. G. Haywood, A. R. Kneller, L. Selzer, A. Zlotnick and S. C. Jacobson, *Anal. Chem.*, 2015, **87**, 699–705.
23 P. Kondylis, J. Zhou, Z. D. Harms, A. R. Kneller, L. S. Lee, A. Zlotnick and S. C. Jacobson, *Anal. Chem.*, 2017, **89**, 4855–4862.
24 J. Zhou, P. Kondylis, D. G. Haywood, Z. D. Harms, L. S. Lee, A. Zlotnick and S. C. Jacobson, *Anal. Chem.*, 2018, **90**, 7267–7274.
25 M. Zhang, Z. D. Harms, T. Greibe, C. A. Starr, A. Zlotnick and S. C. Jacobson, *ACS Nano*, 2022, **16**, 7352–7360.
26 T. W. Young, M. P. Kappler, N. M. Hockaden, R. L. Carpenter and S. C. Jacobson, *Anal. Chem.*, 2023, **95**, 16710–16716.
27 T. W. Young, M. P. Kappler, E. D. Call, Q. J. Brown and S. C. Jacobson, *Annu. Rev. Anal. Chem.*, 2024, **17**, 221–242.
28 S. Shivanka, F. Shiri, M. Chibuike, C. McKinney, M. Verber, J. Choi, S. Park, A. R. Hall and S. A. Soper, *Sci. Rep.*, 2025, **15**, 13742.
29 S. Pud, S.-H. Chao, M. Belkin, D. Verschueren, T. Huijben, C. van Engelenburg, C. Dekker and A. Aksimentiev, *Nano Lett.*, 2016, **16**, 8021–8028.
30 X. Liu, Y. Zhang, R. Nagel, W. Reisner and W. B. Dunbar, *Small*, 2019, **15**, 1901704.
31 A. Bhattacharya and S. Seth, *Phys. Rev. E*, 2020, **101**, 052407.

32 A. Choudhary, H. Joshi, H.-Y. Chou, K. Sarthak, J. Wilson, C. Maffeo and A. Aksimentiev, *ACS Nano*, 2020, **14**, 15566–15576.
33 A. Bhattacharya, *J. Phys.: Conf. Ser.*, 2021, **2122**, 012003.
34 Z. Liu, W. Dong, T. St-Denis, M. A. S. Pessôa, S. Shiekh, P. Ravikumar and W. Reisner, *DNA Dynamics in Dual Nanopore Tug-of-War*, 2025, https://arxiv.org/abs/2508.21144.
35 P. Cadinu, B. P. Nadappuram, D. J. Lee, J. Y. Y. Sze, G. Campolo, Y. Zhang, A. Shevchuk, S. Ladame, T. Albrecht, Y. Korchev, A. P. Ivanov and J. B. Edel, *Nano Lett.*, 2017, **17**, 6376–6384.
36 P. Cadinu, G. Campolo, S. Pud, W. Yang, J. B. Edel, C. Dekker and A. P. Ivanov, *Nano Lett.*, 2018, **18**, 2738–2745.
37 P. Cadinu, M. Kang, B. P. Nadappuram, A. P. Ivanov and J. B. Edel, *Nano Lett.*, 2020, **20**, 2012–2019.
38 J. E. Hall, *J. Gen. Physiol.*, 1975, **66**, 531–532.
39 Y. Green, R. Abu-Rjal and R. Eshel, *Phys. Rev. Appl.*, 2020, **14**, 014075.
40 S. Garaj, W. Hubbard, A. Reina, J. Kong, D. Branton and J. A. Golovchenko, *Nature*, 2010, **467**, 190–193.
41 G. F. Schneider, S. W. Kowalczyk, V. E. Calado, G. Pandraud, H. W. Zandbergen, L. M. K. Vandersypen and C. Dekker, *Nano Lett.*, 2010, **10**, 3163–3167.
42 C. A. Merchant, K. Healy, M. Wanunu, V. Ray, N. Peterman, J. Bartel, M. D. Fischbein, K. Venta, Z. Luo, A. T. C. Johnson and M. Drndić, *Nano Lett.*, 2010, **10**, 2915–2921.
43 T. Jain, B. C. Rasera, R. J. S. Guerrero, M. S. H. Boutilier, S. C. O'Hern, J. C. Idrobo and R. Karnik, *Nat. Nanotechnol.*, 2015, **10**, 1053–1057.
44 J. Feng, M. Graf, K. Liu, D. Ovchinnikov, D. Dumcenco, M. Heiranian, V. Nandigana, N. R. Aluru, A. Kis and A. Radenovic, *Nature*, 2016, **536**, 197–200.
45 L. Wang, M. S. H. Boutilier, P. R. Kidambi, D. Jang, N. G. Hadjiconstantinou and R. Karnik, *Nat. Nanotechnol.*, 2017, **12**, 509–522.
46 S. Sahu and M. Zwolak, *Rev. Mod. Phys.*, 2019, **91**, 021004.
47 L. Mogg, S. Zhang, G. P. Hao, K. Gopinadhan, D. Barry, B. L. Liu, H. M. Cheng, A. K. Geim and M. Lozada-Hidalgo, *Nat. Commun.*, 2019, **10**, 4243.
48 G. Danda and M. Drndić, *Curr. Opin. Biotechnol.*, 2019, **55**, 124–133.
49 S. Faucher, N. Aluru, M. Z. Bazant, D. Blankschtein, A. H. Brozena, J. Cumings, J. P. de Souza, M. Elimelech, R. Epsztein, J. T. Fourkas, A. G. Rajan, H. J. Kulik, A. Levy, A. Majumdar, C. Martin, M. McEldrew, R. P. Misra, A. Noy, T. A. Pham, M. Reed, E. Schwegler, Z. Siwy, Y. Wang and M. Strano, *J. Phys. Chem. C*, 2019, **123**, 21309–21326.
50 N. Kavokine, R. R. Netz and L. Bocquet, *Annu. Rev. Fluid Mech.*, 2021, **53**, 377–410.
51 N. R. Aluru, F. Aydin, M. Z. Bazant, D. Blankschtein, A. H. Brozena, J. P. de Souza, M. Elimelech, S. Faucher, J. T. Fourkas, V. B. Koman, M. Kuehne, H. J. Kulik, H.-K. Li, Y. Li, Z. Li, A. Majumdar, J. Martis, R. P. Misra, A. Noy, T. A. Pham, H. Qu, A. Rayabharam, M. A. Reed, C. L. Ritt, E. Schwegler, Z. Siwy, M. S. Strano, Y. Wang, Y.-C. Yao, C. Zhan and Z. Zhang, *Chem. Rev.*, 2023, **123**, 2737–2831.
52 I. Rubinstein and F. Maletzki, *J. Chem. Soc., Faraday Trans.*, 1991, **87**, 2079–2087.
53 Y. Green, Y. Edri and G. Yossifon, *Phys. Rev. E*, 2015, **92**, 033018.
54 J. Sebastian and Y. Green, *Adv. Phys. Res.*, 2023, **2**, 2300044.
55 S. A. Mareev, V. S. Nichka, D. Y. Butylskii, M. K. Urtenov, N. D. Pismenskaya, P. Y. Apel and V. V. Nikonenko, *J. Phys. Chem. C*, 2016, **120**, 13113–13119.
56 R. Holm, *Electric contacts: theory and application*, Springer-Verlag, Berlin Heidelberg, Germany, 4th edn, 1967.
57 R. S. Timsit, *J. Phys. D: Appl. Phys.*, 1977, **10**, 2011.
58 I. Rubinstein, *Phys. Fluids*, 1991, **3**, 2301–2309.
59 I. Rubinstein, B. Zaltzman and T. Pundik, *Phys. Rev. E*, 2002, **65**, 041507.
60 Y. Green and G. Yossifon, *Phys. Rev. E*, 2014, **89**, 013024.
61 Y. Green, S. Shloush and G. Yossifon, *Phys. Rev. E*, 2014, **89**, 043015.
62 Y. Green, R. Eshel, S. Park and G. Yossifon, *Nano Lett.*, 2016, **16**, 2744–2748.
63 G. Yossifon, P. Mushenheim, Y.-C. Chang and H.-C. Chang, *Phys. Rev. E*, 2009, **79**, 046305.
64 G. Yossifon, P. Mushenheim, Y.-C. Chang and H.-C. Chang, *Phys. Rev. E*, 2010, **81**, 046301.
65 G. Yossifon, P. Mushenheim and H.-C. Chang, *Europhys. Lett.*, 2010, **90**, 64004.
66 A. Gray and G. B. Mathews, *A treatise on Bessel functions and their applications to physics*, Macmillan and Co., London, UK, 1895.
67 A. M. Rosenfeld and R. S. Timsit, *Q. Appl. Math.*, 1981, **39**, 405–417.
68 R. S. Timsit, in *Electrical Contact Resistance: Fundamental Principles*, ed. P. G. Slade, CRC Press, Boca Raton, FL, United States, 2nd edn, 2014, pp. 3–112.
69 J. Bair, T. Burkhardt, Z. Gottshall and M. Kuehne, Coupling Effects on Access Resistance of In-Series Nanopores, 2025, DOI: 10.5281/zenodo.18940627.